nature materials

Article

https://doi.org/10.1038/s41563-023-01473-9

Chiral-phonon-activated spin Seebeck effect

Received: 10 June 2021

Accepted: 9 January 2023

Published online: 13 February 2023

Check for updates

Kyunghoon Kim ^{1,2,6}, Eric Vetter^{2,3,6}, Liang Yan ^{2,4,6}, Cong Yang^{1,2,6}, Ziqi Wang^{1,2}, Rui Sun^{2,3}, Yu Yang⁵, Andrew H. Comstock ^{2,3}, Xiao Li⁵, Jun Zhou⁵, Lifa Zhang ⁵⊠, Wei You ^{2,4}⊠, Dali Sun ^{3,2}⊠ & Jun Liu ^{1,2}⊠

Utilization of the interaction between spin and heat currents is the central focus of the field of spin caloritronics. Chiral phonons possessing angular momentum arising from the broken symmetry of a non-magnetic material create the potential for generating spin currents at room temperature in response to a thermal gradient, precluding the need for a ferromagnetic contact. Here we show the observation of spin currents generated by chiral phonons in a two-dimensional layered hybrid organic–inorganic perovskite implanted with chiral cations when subjected to a thermal gradient. The generated spin current shows a strong dependence on the chirality of the film and external magnetic fields, of which the coefficient is orders of magnitude larger than that produced by the reported spin Seebeck effect. Our findings indicate the potential of chiral phonons for spin caloritronic applications and offer a new route towards spin generation in the absence of magnetic materials.

The interplay between spin and heat currents, comprising the field of spin caloritronics^{1,2}, enables the versatile conversion of heat currents into spin currents and vice versa in various magnetic materials³⁻¹⁰. One of the prototypical phenomena in spin caloritronics is the spin Seebeck effect that occurs in ferromagnetic insulators, antiferromagnetic insulators, paramagnets and magnetic semiconductors $^{4,6,9,11-14}$, which can be considered as a spin analogue to the Seebeck effect in thermoelectrics. The spin Seebeck effect unites two types of coupled bosonic collective excitations, that is, phonons and magnons¹⁵, when a magnetic material is subject to a thermal gradient (∇T). The spin Seebeck effect leads to the generation of non-equilibrium spin currents (a flow of spin angular momentum) in an attached conductor parallel to the direction of the thermal gradient (Fig. 1a). The spin current is subsequently converted to a measurable transverse electric voltage via the inverse spin Hall effect^{4,6,16}. The spin Seebeck effect has been shown to be associated with the non-equilibrium transfer of spin angular momentum to the attached conductor via coupling between magnons and 'spinless' phonons¹⁵. An outstanding question is whether or not 'only' phonons with quantized non-zero angular momentum can also generate spin current.

Chirality is a geometrically distinguishable property of a system that does not possess inversion symmetry, that is, a mirror plane or glide plane symmetry! In addition, phonons can attain intrinsic chirality (that is, chiral phonons 18,19), as revealed recently in an atomic lattice of monolayer WSe $_2$ (refs. 20,21). Induced by the broken inversion symmetry of the two-dimensional (2D) hexagonal lattice of WSe $_2$, the degeneracy of clockwise and counterclockwise phonon modes is lifted in the absence of external magnetic fields, exhibiting well-defined angular momentum that can be transferred and alter the spin states of excited electrons or holes via electron–phonon and optical scatterings. It is then natural to propose a scenario where the propagating chiral phonons 22 can transfer their angular momentum and drive a non-equilibrium spin current in an adjacent conductor in the same way as the spin Seebeck effect but without the need for magnetic elements (Fig. 1b).

Here we report the observation of a chiral-phonon-activated spin Seebeck (CPASS) effect in non-magnetic 2D chiral hybrid organic–inorganic perovskite (chiral HOIP) materials by applying a transient temperature gradient induced using ultrafast laser pulses. The generation

¹Department of Mechanical and Aerospace Engineering, North Carolina State University, Raleigh, NC, USA. ²Organic and Carbon Electronics Laboratories (ORaCEL), North Carolina State University, Raleigh, NC, USA. ³Department of Physics, North Carolina State University, Raleigh, NC, USA. ⁴Department of Chemistry, University of North Carolina at Chapel Hill, Chapel Hill, NC, USA. ⁵School of Physics and Technology, Nanjing Normal University, Nanjing, China. ⁶These authors contributed equally: Kyunghoon Kim, Eric Vetter, Liang Yan, Cong Yang. ⊠e-mail: phyzlf@njnu.edu.cn; wyou@unc.edu; dsun4@ncsu.edu; jliu38@ncsu.edu

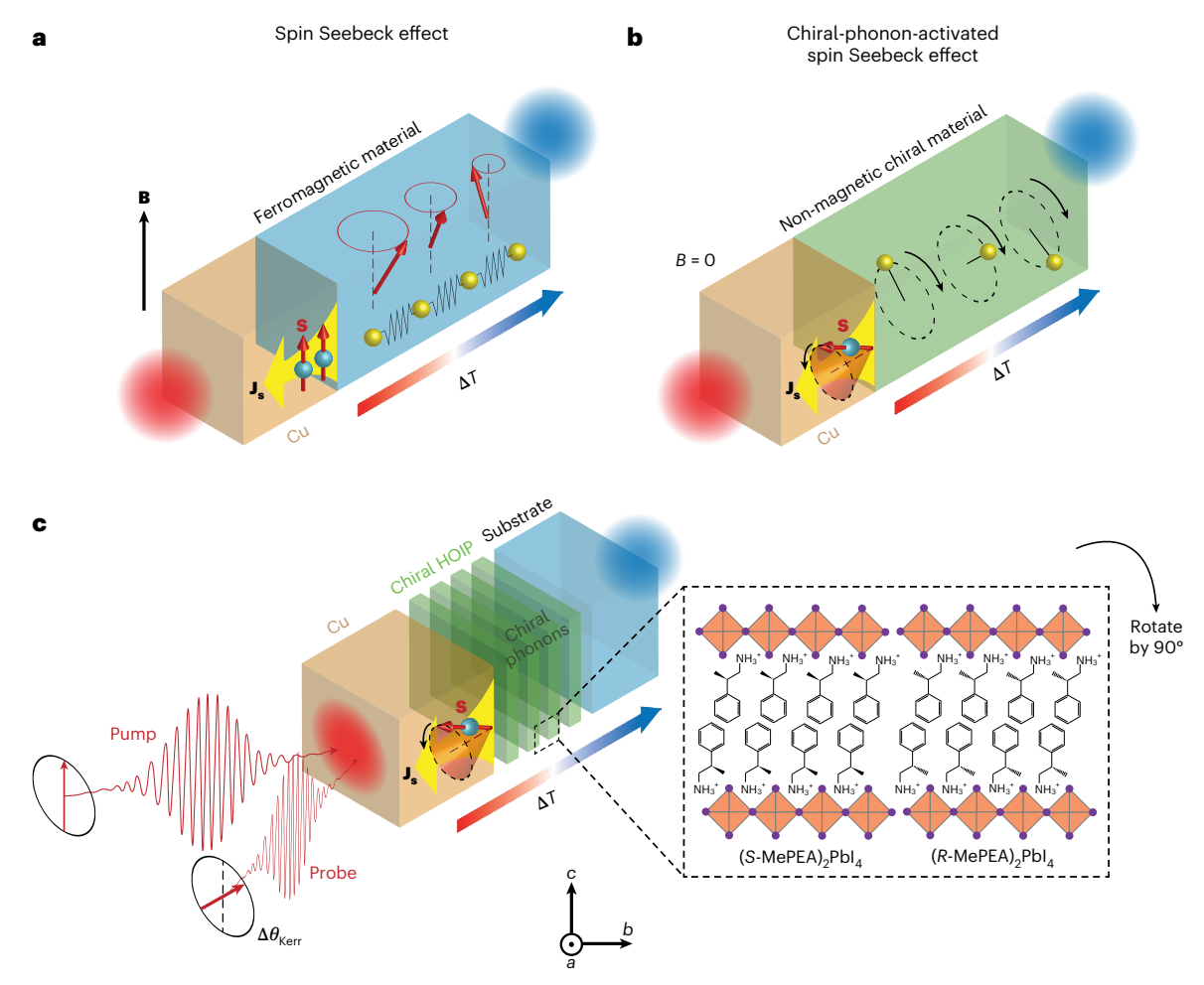


Fig. 1|Spin Seebeck effect, chiral-phonon-activated spin Seebeck effect (CPASS) and experimental setup. a, Schematic illustration of the spin Seebeck effect in a ferromagnetic material. By applying a temperature gradient to the ferromagnet (the red and blue spheres represent the hot and cold end, respectively), a spin current J_s is generated in an adjacent non-magnetic layer (that is, Cu). The spin polarization of the generated spin current S (represented by a red arrow with a blue sphere at the center) is parallel to the magnetization of the ferromagnet under an external magnetic field, B. The red arrows represent the propagation of magnons under the thermal gradient; the yellow spheres and springs represent the vibrational modes of atoms (conventional phonons) in the ferromagnetic material. b, Schematic illustration of the CPASS effect. When a temperature difference ΔT is applied to a chiral material, a spin current can be produced in the Cu layer due to the propagation of the

chiral phonons through the material in the absence of the magnetization and magnetic field. The circular rotational motion of yellow spheres represents chiral phonon. \mathbf{c} , Measurement geometry (not to scale) of the CPASS effect in layered Cu/chiral HOIP heterostructures using the TR-MOKE technique. The expanded panel shows a schematic of the 2D chiral HOIP structure used in this work, which consists of an alternating lead halide framework and chiral organic ligands with opposite chirality. An ultrafast temperature gradient is built across the heterostructure using a laser pump pulse that is incident on the Cu layer. The diffusive spin current in the Cu layer that is generated via the CPASS effect is detected using a probe pulse, where the polarization of light (the red arrows associated with the pump and probe pulses) rotates by an amount of $\Delta\theta_{kerr}$, that is, the Kerr rotation angle.

of a transient spin current via chiral phonons is probed in an adjacent non-magnetic conductor via time-resolved magneto-optical Kerr effect (TR-MOKE) measurements 23 . We found that the generated spin current, $\mathbf{J_s}$, can persist for up to -4 ns with an oscillating spin polarization vector, \mathbf{S} , in the gigahertz frequency range, and that the phase of the generated spin current is strongly associated with the chirality of the HOIP film. This spin current is further confirmed by exerting a spin-transfer torque (STT) on an adjacent magnetic layer that leads to subsequent precession of the magnetization 24,25 . Notably, we unveil a time-dependent helical-like spin polarization vector of the spin current induced by the CPASS effect along the chiral axis (Fig. 1b). The CPASS-induced spin current shows a strong magnetic field dependence, implying tunable electron spin–phonon coupling at the interface driven by the thermal gradient.

A schematic overview of our experiment is described in Fig. 1c. We prepared a heterostructure consisting of a non-magnetic

layer (that is, Cu) adjacent to a chiral material in the absence of magnetic elements (see Methods). The chiral materials used in the present study are solution-processed 2D layered chiral HOIPs (that is, (S-MePEA)₂PbI₄ or (R-MePEA)₂PbI₄, where MePEA is β-methylphenylethylamine) that were spun-cast onto a Si substrate²⁶⁻²⁸. Schematics of the crystal structures of the 2D chiral HOIPs are illustrated in Fig. 1c. They consist of alternating layers of organic compounds and an inorganic framework of corner-sharing metal halide octahedra^{29,30}. The chirality of the chiral HOIP films originates from the implanted chiral organic ligands inserted between the inorganic layers, as validated via their circular dichroism spectra (Supplementary Fig. 1). The orientation of the prepared thin film was examined using X-ray diffraction (Supplementary Fig. 2), showing that the layered structure is textured with the *c*-axis normal to the film plane³¹. The non-magnetic Cu layer is deposited on top of the prepared chiral HOIP films using electron-beam evaporation.

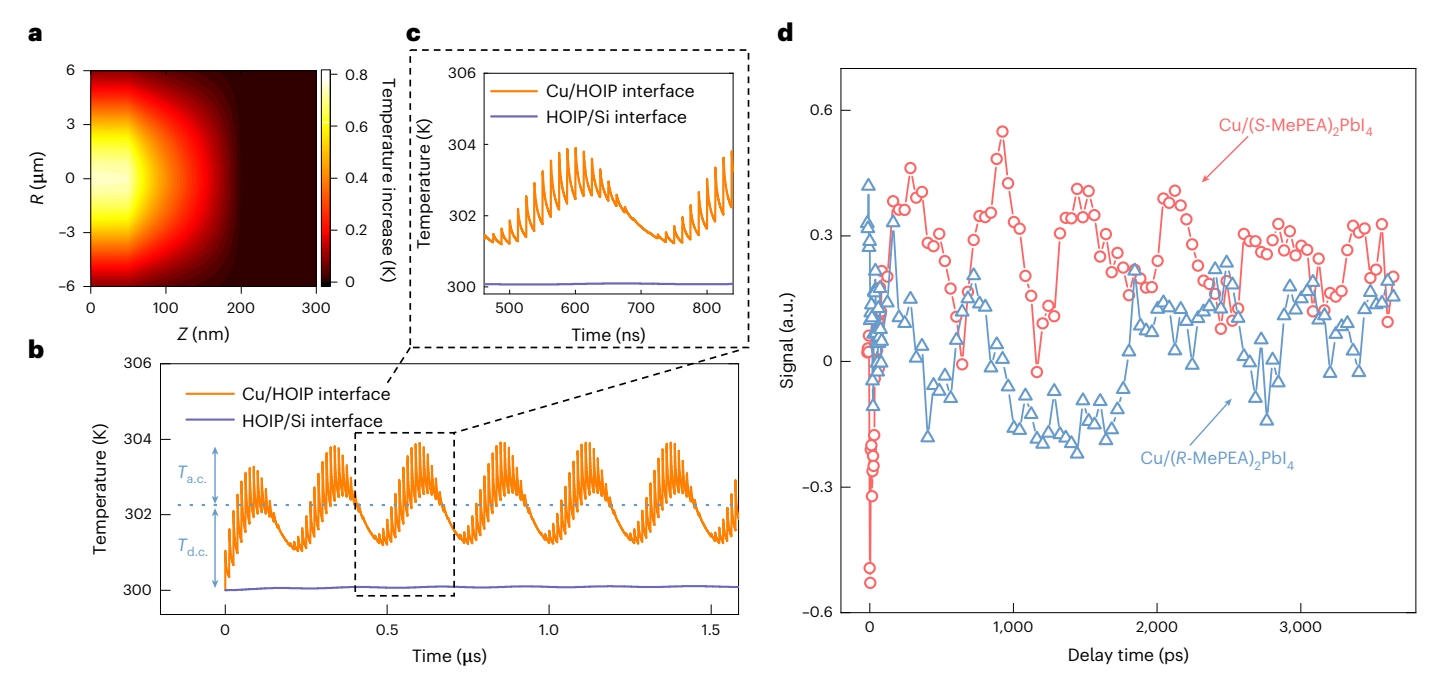


Fig. 2| **Transient spin current generation.** a–c, Spatial (a) and transient (b,c) temperature gradient created across the heterostructure in the TR-MOKE measurement obtained from the TDTR measurements and thermal modelling. R is the radial coordinate from the laser beam center; Z is the depth from the sample surface (that is, Cu surface); $T_{a.c.}(T_{d.c.})$ is the a.c. (d.c.) temperature rise created

by the laser pulses. ${f d}$, Transient Kerr rotation signals measured, respectively, on the Cu layer side of the Cu/(S-MePEA) $_2$ PbI $_4$ (blue) and Cu/(R-MePEA) $_2$ PbI $_4$ (red) heterostructure. The laser-induced change in the Kerr rotation in each heterostructure is plotted as a function of the time delay. All measurements were performed at room temperature without applying a magnetic field.

A pump laser pulse excites the Cu layer and creates a transient thermal gradient throughout the whole heterostructure from the top Cu layer to the bottom chiral HOIP/Si substrate. The heat current flows along the thermal gradient inside the chiral HOIP film, which drives the propagation of chiral phonons. Interacting with electrons, the chiral phonons generate a spin current without the need for an applied magnetic field. The spin current accumulates in the Cu layer and diffuses to the top surface with a spin polarization direction that is dependent on the chirality of the chiral HOIP film. Here both pump and probe beams are incident on the same Cu side of the sample, and polar TR-MOKE measurements (see Methods) are used to detect the transient spin accumulation at the Cu side along the normal direction³². A relatively thick Cu layer (≈50 nm) is chosen to ensure (1) that the absorption of the pump laser is confined to the metallic layer within the optical penetration depth (≈12 nm (ref. ³³)) so that only the heat current transmits across the whole heterostructure, (2) measurement of the spin accumulation only on the surface of the Cu layer that is not subject to parasitic Faraday signals produced from the HOIP film itself, and (3) adequate Kerr signal sensitivity under a longer spin relaxation time (~16 ps (refs. 32,34)) compared with other large spin-orbit coupling materials, for example, Pt, Au and so on. Using a similar setup, we conducted time-domain thermoreflectance (TDTR) measurements (see Methods) and numerical calculations to determine the transient temperature excursion of the heterostructure and the temperature gradient across the chiral film35,36.

Generation of an oscillating spin current via the CPASS effect

Figure 2a–c depicts a schematic overview of the transient and spatial thermal response in the Cu/chiral HOIP heterostructure upon irradiation using a sequence of pump laser pulses. The transient temperature response in this sample is distinctively different from an all-metallic bilayer sample, that is, a Cu/Ni control sample. In the Cu/Ni sample, the ultrashort laser pulse excites the Cu layer and results in the fast

transport of thermal energy from the Cu side to the Ni layer. Owing to the high thermal conductivities in metals, the transient temperature gradient is established rapidly on a picosecond timescale (Supplementary Fig. 11). By contrast, in the Cu/chiral HOIP sample, the thermal energy deposited by the pump pulses decays slowly on an order longer than the nanosecond timescale due to the low thermal conductivity of the HOIP layer. In addition to an alternating current (a.c.) transient temperature gradient modulated by each pump pulse, the accumulation of the thermal energy deposited after a series of pump pulses creates a non-negligible persistent direct current (d.c.) temperature gradient across the entire sample (illustrated in Fig. 2b).

Figure 2d shows the time-resolved Kerr rotation signals probed on the Cu side of the two different types of chiral-HOIP-based heterostructure that have opposite chirality, that is, Cu/(S-MePEA)₂PbI₄ (~150 nm) and Cu/(R-MePEA)₂PbI₄ (~150 nm). After a sharp change in the Kerr signal within a few picoseconds, a long-lived oscillating Kerr signal around the gigahertz frequency (~2 GHz) is observed, exhibiting a slow decay that persists up to ~4 ns. No similar Kerr response is detected in the Cu/ Si or Cu/non-chiral/Si control sample, thereby excluding the possible birefringence effect in the metallic layer upon the high-energy laser heating. We found that when the chirality of the HOIP films changes from left-handed (S, red) to the right-handed (R, blue), the phase of the oscillating Kerr signal is inverted. Compared with the transient Kerr signal caused by the ultrafast spin-dependent spin Seebeck effect²⁵ that is measured in a control Cu/Ni/SiO₂/Si sample (Supplementary Fig. 4) using the same setup, here we conclude that the observed Kerr signal is caused by spin accumulation in the Cu layer induced by the a.c. thermal gradient. It is noteworthy that the diffusive spin propagation velocity is of the order of 100 nm ps⁻¹; therefore, the transient time across the 50-nm-thick Cu layer takes less than 0.5 ps (ref. 32). Thus, the observed transient spin signal at a timescale of subnanoseconds to a few nanoseconds implies a long-lasting spin current generation process via the CPASS effect. This is in contrast to the rapidly decayed spin current in all-metallic heterostructures driven by the ultrafast demagnetization

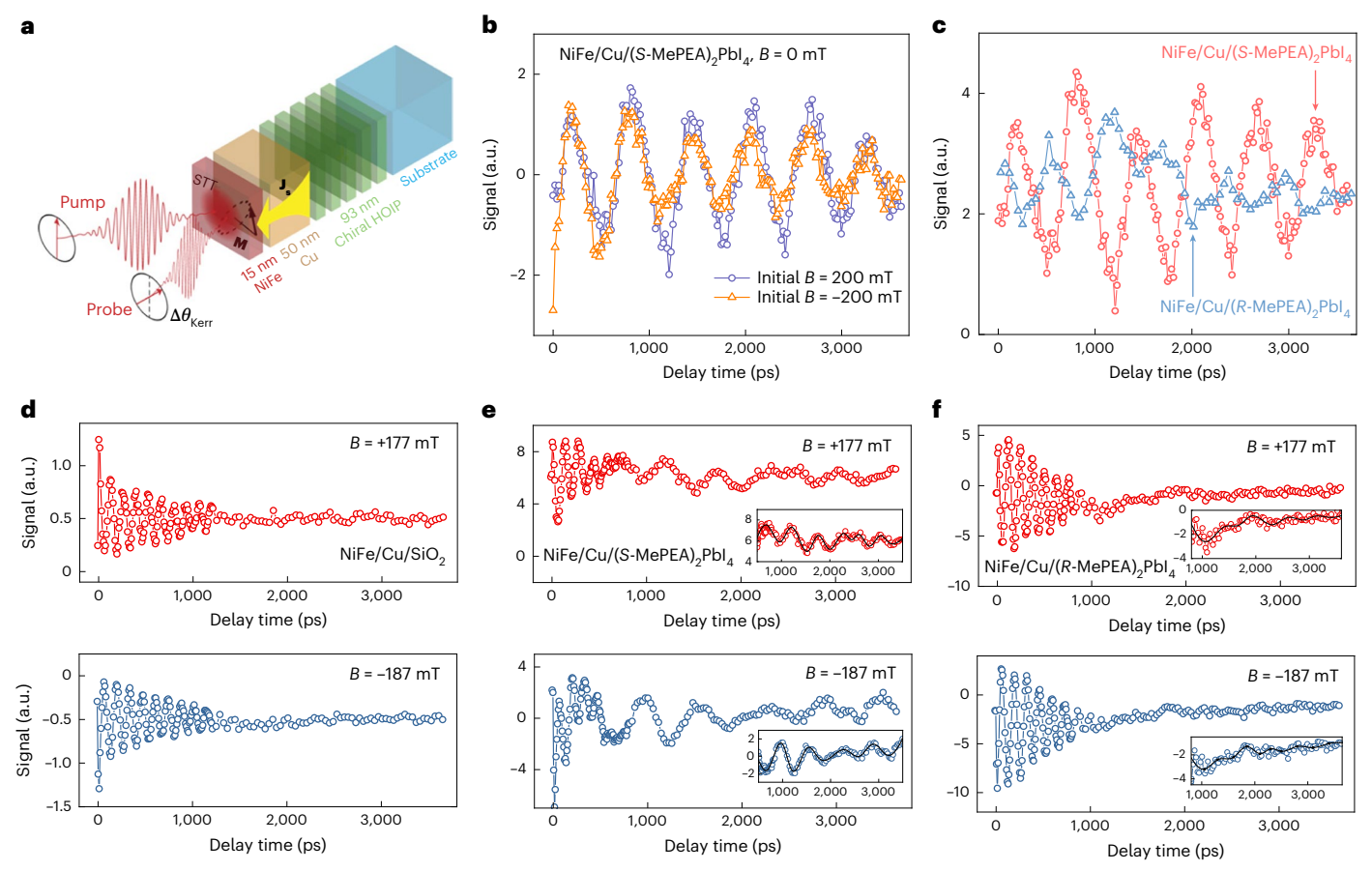


Fig. 3 | **CPASS-driven STT. a**, Schematic illustration of the STT device configuration and the precession motion of the magnetization **M** in the NiFe layer due to the STT exerted by the injected spin current through the Cu layer. **b**, Transient Kerr rotation signal measured in NiFe/Cu/(S-MePEA) $_2$ PbI $_4$ at zero field (B=0 mT) when the NiFe layer is at the opposite magnetic remanence. **c**, Same data as in **b** but for the respective NiFe/Cu/(R- or S-MePEA) $_2$ PbI $_4$ devices

with different chiralities. $\mathbf{d}-\mathbf{f}$, Transient Kerr rotation signals measured in the NiFe-only sample (\mathbf{d}) , the NiFe/Cu/(S-MePEA)₂PbI₄ device (\mathbf{e}) and the NiFe/Cu/(R-MePEA)₂PbI₄ device (\mathbf{f}) while applying an external magnetic field at an angle of 70° with respect to the film plane $(B \approx \pm 180 \text{ mT})$, respectively. The insets in \mathbf{e} and \mathbf{f} present the zoomed-in STT signals on the long timescale (t > 1 ns). Solid lines in the insets are added to guide the eye.

on a subpicosecond timescale 23 or the spin-dependent Seebeck effect on a timescale of several picoseconds 25 . Furthermore, since the polar TR-MOKE setup is more sensitive to the out-of-plane spin polarization, the oscillating feature of the spin current unveils a discernible and rich electron spin-phonon coupling that is driven by the chiral phonons in chiral materials 37,38 , in sharp contrast to the monotonically fast decay of spin signals (within 15 ps) caused by the chirality-induced spin selectivity (CISS) effect in chiral HOIP materials 28 .

CPASS-driven spin-transfer torque

To validate the spin current generated by the CPASS effect in response to a temperature gradient, we seek to provide unambiguous evidence by examining the torque exerted on an adjacent ferromagnetic layer induced by the generated spin current, that is, an ultrafast STT 25 . The STT device configuration is illustrated in Fig. 3a, and consists of an extra ferromagnetic thin layer of NiFe (permalloy, ≈ 15 nmthick) added on top of the Cu (≈ 50 nm)/chiral HOIP heterostructures. Presumably, the CPASS-driven spin current has an out-of-plane spin polarization that is partially transverse to the magnetization of the NiFe layer when a tilted external magnetic field is applied. By absorbing this spin current, the NiFe layer acts as a spin sink via the STT process, leading to a precessional motion of magnetization that will be detected via the polar TR-MOKE measurements. The magnetization dynamics of the NiFe layer can be described using the Landau–Lifshitz–Gilbert–Slonczeswki equation that incorporates STT terms 39 :

$$\frac{\mathrm{d}\mathbf{m}(t)}{\mathrm{d}t} = -\gamma \mathbf{m}(t) \times \mathbf{B} + \alpha \mathbf{m}(t) \times \frac{\mathrm{d}\mathbf{m}(t)}{\mathrm{d}t} + \frac{h\gamma}{4\pi e M_{s} d} \mathbf{m}(t) \times [\mathbf{m}(t) \times \mathbf{J}_{s}(t)],$$
(1)

where $\mathbf{m}(t)$ and $\mathbf{J}_{\mathbf{s}}(t)$ are the time-dependent unit vectors of the magnetization of the NiFe layer and injected spin current density, respectively. Here, we simplified the notation for the spin current density because all the spin currents in our setup flow along the z direction (see the full notation in Supplementary Equation (10)). The spin current density vector $\mathbf{J}_{s}(t)$ has three components, where $J_{sy}J_{sy}$ and J_{sz} represent the respective amplitude of the oscillation along each spin polarization direction. B is the applied external magnetic field, γ is the gyromagnetic ratio, h is the Planck constant and α is the Gilbert damping constant. The third term on the right-hand side of equation (1) presents the damping-like STT contribution³⁹. e is the elementary charge. M_s and d are the saturation magnetization and thickness of the NiFe layer, respectively. Figure 3b presents direct evidence of the CPASS-driven STT by measuring the time-resolved Kerr signal on the NiFe layer of the NiFe/Cu/(S-MePEA)₂PbI₄ sample at zero field (B = 0 mT). A clear long-lived oscillating Kerr signal is observed in the same gigahertz frequency (~2 GHz), consistent with that in Fig. 2d. It is noteworthy that no precessional motion of the magnetization is expected in the absence of the external magnetic field (Supplementary Fig. 12). The oscillating Kerr signals validate the ultrafast STT signals that are driven by the time-dependent spin current injection via the CPASS effect.

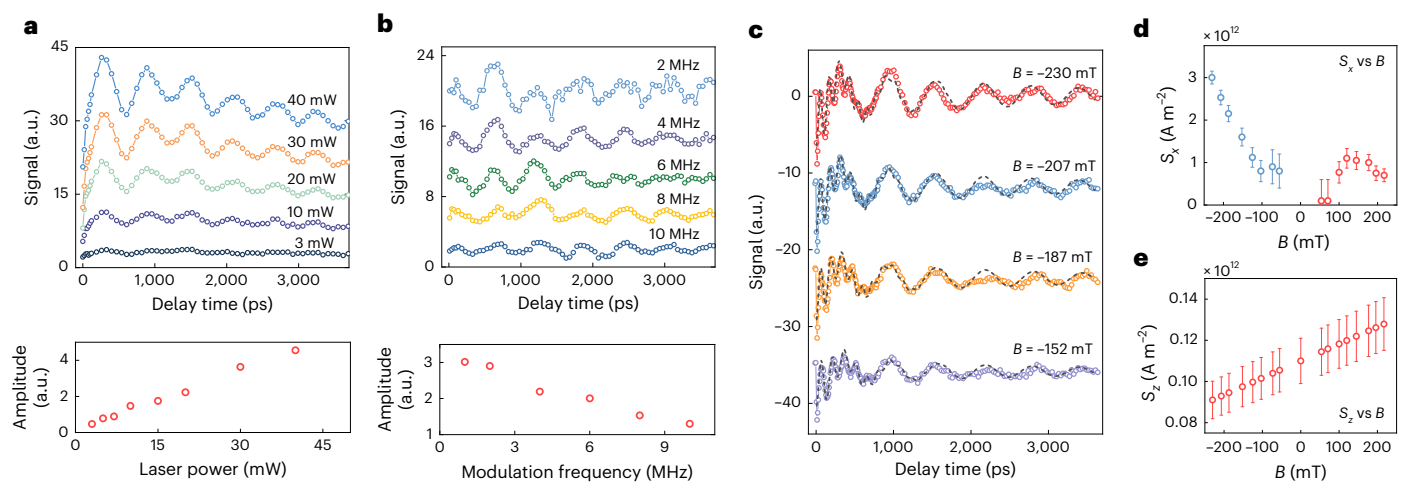


Fig. 4 | Power, modulation and magnetic field dependence. a,b, Laser power (a) and modulation frequency (b) dependence of the transient STT signals measured at zero field in the NiFe/Cu/(S-MePEA)₂PbI₄ device. The bottom panels show the obtained precession amplitude of the STT signal as a function of the laser power and modulation, respectively. c, Transient Kerr rotation signals measured in the NiFe/Cu/(S-MePEA)₂PbI₄ device at different magnetic fields.

Fitted precessions that include both FMR and STT modes are plotted (dashed lines). Signals in $\mathbf{a} - \mathbf{c}$ are shifted vertically for clarity. \mathbf{d} , \mathbf{e} , Calculated field-dependent spin current density polarized along the x direction (S_x) (\mathbf{d}) and the z direction (S_z) (\mathbf{e}). Data are presented as the mean \pm standard deviation. The error bars are determined from the fits of the raw data in \mathbf{c} .

By inverting the magnetization direction of the NiFe at the remanence (initially polarized at +B/-B), the non-shifted phase of the precessional Kerr signals implies that the damping-like term dominates the STT process, as reported elsewhere²⁵. The precessional phase of the Kerr signals indeed shifts when the chirality of the HOIP layer is inverted. Figure 3c shows that the phase of the oscillating Kerr signals inverts at zero field when the chirality is flipped, which is consistent with the observation in Fig. 2d.

Figure 3e,f shows the measured time-resolved Kerr signal in the NiFe/Cu/(S- or R-MePEA)₂PbI₄ samples, respectively, by applying a tilted magnetic field $B \approx \pm 180$ mT (70° normal to the sample film plane), alongside a comparison with the NiFe-only sample in Fig. 3d. With pump laser excitation, two types of precessions in the NiFe layer are revealed. (1) On a short timescale (t < 1 ns), both R and S chiral samples exhibit a high-frequency precession caused by ultrafast demagnetization and remagnetization of the NiFe layer at the ferromagnetic resonance (FMR) condition, defined as the 'FMR mode'. The field dependence of the precession frequency in all the samples is plotted in Supplementary Fig. 15, which follows the Kittel equation, similar to that in the NiFe-only sample 40 . (2) On a long timescale (t > 1 ns), a second precession at a lower frequency of ~2 GHz is observed that is attributed to the CPASS-driven STT (defined as the 'STT mode'), coinciding with the observations at zero field shown in Fig. 3c. The oscillating amplitude of the STT mode in the chiral S sample is comparable to that of the FMR mode, implying that an efficient STT occurred in the NiFe layer. The much weaker oscillation amplitude in the chiral R sample can be explained by the decreased circular dichroism signal in the chiral R HOIP films (Supplementary Fig. 1), as corroborated in Fig. 3c. Surprisingly, we found that the phase of the STT mode is reversed when the magnetic field direction is inverted, that is, in contrast to the case at zero field, indicating a strongly field-dependent phase of the spin current generation via the CPASS effect. Such a strong field dependence is also observed in the spin accumulation results on the Cu-based sample, where the amplitude of the spin current with an out-of-plane polarization J_{sz} is detected (Supplementary Fig. 13).

Estimation of the CPASS coefficient

Below we calculate the spin current generation via the CPASS effect based on the results obtained from the both Cu-based and STT sample structures that can be described as:

$$|\mathbf{J}_{\mathbf{s}}| = S_{\text{CPASS}} |\nabla T|, \qquad (2)$$

where $|\nabla T|$ is the magnitude of the temperature gradient generated across the sample structure induced by ultrafast laser heating. The CPASS coefficient is defined as $S_{CPASS} = |\mathbf{J}_{s}|/|\nabla T|$ in the units of A (K m)⁻¹. The transient spin current generation may consist of two components: (1) a relatively fast spin current as a result of the chiral phonons near the Cu/chiral HOIP interface that quickly respond to the a.c. temperature modulation, $\nabla T_{a.c.}$, induced by a single pump pulse (Fig. 2c); and (2) a slow spin accumulation driven by the delayed chiral phonons propagating inside the bulk chiral HOIP layer in the presence of the d.c. temperature gradient, ∇T_{dc} . To separate these two components, the dependence of the STT signal on the laser power and the modulation frequency is studied. Figure 4a shows the time-resolved Kerr signal at different incident laser powers measured in the NiFe/Cu/(S-MePEA)₂PbI₄ sample for the zero-field condition. When plotting the normalized Kerr signal as a function of the incident laser power, we found that the amplitude of the STT signal ($\propto |\mathbf{J}_s|$) scales linearly with the incident power. This linear relation is confirmed by the calculated a.c. and d.c. temperature gradients, which should be linearly proportional to the incident laser power (details on the determination of the thermal properties of the chiral HOIP films, the temperature profiles across these films, and the a.c. and d.c. temperature gradients are described in Supplementary Figs. 5–10). This linearity is similar to spin generation from the conventional spin Seebeck effect, where the spin Seebeck coefficient does not depend on the temperature gradient^{4,41}. When varying the a.c. modulation frequency of the pump laser (Fig. 4b), the increased amplitude of the Kerr signal at lower modulation frequencies suggests that the a.c. temperature gradient dominates the CPASS effect since the d.c. temperature gradient is independent of the modulation frequency (Supplementary Fig. 10).

To extract the amplitude of the generated spin current density at different polarities, time-resolved STT signals of the chiral S samples were measured at different magnetic fields, as shown in Fig. 4c. Both the amplitude and phase of the STT mode change as a function of the external magnetic field (Supplementary Fig. 16). The dashed lines in each plot denote the fits of the data by solving equation (1) in the values of $\mu_0 M_s = 0.96$ T, $\alpha = 0.039$, d = 15 nm and $\gamma = 1.8 \times 10^{11}$ rad (s T)⁻¹ for the NiFe layer⁴², where μ_0 is the vacuum magnetic permeability. We found

that an oscillating spin current component containing both the in-plane $(I_{sx}$ and $I_{sy})$ and out-of-plane spin polarization (I_{sx}) directions needs to be considered, from which the amplitudes of these polarized and oscillating spin current densities are respectively derived as a function of the magnetic field. The CISS mechanism (only a non-oscillating value of I_{cz}) can again be ruled out due to the completely different field dependence of the precessional amplitude and phase (see the detailed discussion and spin current expression in Supplementary Figs. 16 and 17, and an animation of the time-dependent spin current in Supplementary Video 1). Both I_{sy} and I_{sy} exhibit an asymmetric field dependence with respect to the field direction (Supplementary Section 5), which is one of the unique features for the CPASS effect, in contrast to the conventional CISS effect^{28,43} that produces a field-independent I_{c2} only along with the chiral axis. At B = -230 mT, a large value of $I_{ex} = (3.00 \pm 0.15) \times 10^{12} \text{ A m}$ ⁻² is obtained that is roughly one order of magnitude higher than the out-of-plane polarized component $(J_{sz} = (0.09 \pm 0.01) \times 10^{12} \text{ A m}^{-2})$. For simplicity, using the obtained J_{sz} component ($J_{sz} = 0.11 \times 10^{12} \,\mathrm{A m^{-2}}$) and the a.c. temperature gradient ($|\nabla T_{a.c.}| = 1.65 \times 10^7 \,\mathrm{K} \,\mathrm{m}^{-1}$) at zero field, we estimate that the lower bound of the CPASS coefficient is 6,667 A (K m)⁻¹ in this sample. This value is orders of magnitude higher than most reported conventional spin Seebeck effect coefficients using various magnetic materials (varying between 1.5 and 540 A (K m)⁻¹; see Supplementary Tables 5 and 6 for a comparison), suggesting an efficient electron spin-phonon coupling utilizing chiral phonons.

In summary, we experimentally demonstrate and validate the generation of spin currents in adjacent metallic layers attached to a non-magnetic chiral material when subjected to a thermal gradient. We explain this observation in the context of the CPASS effect. The demonstrated CPASS effect is separate from the conventional CISS effect^{28,43} as reported widely in different chiral assemblies under electrical excitation, which has been specifically described as a 'spin-filtering' process when electrons transmit through the chiral structure. Instead of creating charge transport across most hydrocarbon-based chiral semiconductor layers that are restricted by moderate electrical conductivities, the CPASS effect provides new opportunities to explore room-temperature spintronic applications by utilizing their structural chirality and leveraging their properties to achieve the energy-efficient transduction of spin information in the absence of electron flow. Moreover, the CPASS effect captures typical experimental CISS features that can be applied not only in low-conductivity chiral semiconductors but also in chiral insulators. Although a complete interpretation of the correlation between structural chirality, chiral phonons and spin still remains open, the CPASS effect provides a viable alternative to guide future CISS theory and elucidate the fundamental understanding of a more 'general' CISS effect⁴⁴ that showcases the importance of thermal dissipation, vibrational modes and the structure-property relationships between spin generation and chirality. By possessing chiral phonons, chiral materials therefore hold great promise as a new class of materials for spin caloritronic applications and energy-harvesting technologies.

Online content

Any methods, additional references, Nature Portfolio reporting summaries, source data, extended data, supplementary information, acknowledgements, peer review information; details of author contributions and competing interests; and statements of data and code availability are available at https://doi.org/10.1038/s41563-023-01473-9.

References

- Bauer, G. E. W., Saitoh, E. & van Wees, B. J. Spin caloritronics. Nat. Mater. 11, 391–399 (2012).
- Hoffmann, A. & Bader, S. D. Opportunities at the frontiers of spintronics. *Phys. Rev. Appl.* 4, 047001 (2015).
- Uchida, K. et al. Observation of the spin Seebeck effect. Nature 455, 778–781 (2008).

- Jaworski, C. M. et al. Observation of the spin-Seebeck effect in a ferromagnetic semiconductor. *Nat. Mater.* 9, 898–903 (2010).
- Slachter, A., Bakker, F. L., Adam, J. P. & van Wees, B. J. Thermally driven spin injection from a ferromagnet into a non-magnetic metal. *Nat. Phys.* 6, 879–882 (2010).
- Uchida, K. et al. Long-range spin Seebeck effect and acoustic spin pumping. Nat. Mater. 10, 737–741 (2011).
- Flipse, J., Bakker, F. L., Slachter, A., Dejene, F. K. & van Wees, B. J. Direct observation of the spin-dependent Peltier effect. Nat. Nanotechnol. 7, 166–168 (2012).
- Jaworski, C. M., Myers, R. C., Johnston-Halperin, E. & Heremans, J. P. Giant spin Seebeck effect in a non-magnetic material. *Nature* 487, 210–213 (2012).
- Wu, S. M., Pearson, J. E. & Bhattacharya, A. Paramagnetic spin Seebeck effect. *Phys. Rev. Lett.* 114, 186602 (2015).
- Meyer, S. et al. Observation of the spin Nernst effect. *Nat. Mater.* 16, 977–981 (2017).
- 11. Uchida, K.-I. et al. Observation of longitudinal spin-Seebeck effect in magnetic insulators. *Appl. Phys. Lett.* **97**, 172505 (2010).
- 12. Seki, S. et al. Thermal generation of spin current in an antiferromagnet. *Phys. Rev. Lett.* **115**, 266601 (2015).
- 13. Wu, S. M. et al. Antiferromagnetic spin Seebeck effect. *Phys. Rev. Lett.* **116**, 097204 (2016).
- Aqeel, A. et al. Spin-Hall magnetoresistance and spin Seebeck effect in spin-spiral and paramagnetic phases of multiferroic CoCr₂O_A films. *Phys. Rev. B* 92, 224410 (2015).
- Xiao, J., Bauer, G. E. W., Uchida, K.-C., Saitoh, E. & Maekawa, S. Theory of magnon-driven spin Seebeck effect. *Phys. Rev. B* 81, 214418 (2010).
- Saitoh, E., Ueda, M., Miyajima, H. & Tatara, G. Conversion of spin current into charge current at room temperature: inverse spin-Hall effect. Appl. Phys. Lett. 88, 182509 (2006).
- Mayer, S. & Kessler, J. Experimental verification of electron optic dichroism. *Phys. Rev. Lett.* 74, 4803–4806 (1995).
- 18. Grissonnanche, G. et al. Chiral phonons in the pseudogap phase of cuprates. *Nat. Phys.* **16**, 1108–1111 (2020).
- Zhang, L. & Niu, Q. Chiral phonons at high-symmetry points in monolayer hexagonal lattices. *Phys. Rev. Lett.* 115, 115502 (2015).
- Zhu, H. et al. Observation of chiral phonons. Science 359, 579–582 (2018).
- Chen, X. et al. Entanglement of single-photons and chiral phonons in atomically thin WSe₂. Nat. Phys. 15, 221–227 (2019).
- Chen, H., Wu, W., Zhu, J., Yang, S. A. & Zhang, L. Propagating chiral phonons in three-dimensional materials. *Nano Lett.* 21, 3060–3065 (2021).
- 23. Choi, G.-M., Min, B.-C., Lee, K.-J. & Cahill, D. G. Spin current generated by thermally driven ultrafast demagnetization. *Nat. Commun.* **5**, 4334 (2014).
- Schellekens, A. J., Kuiper, K. C., de Wit, R. R. J. C. & Koopmans, B. Ultrafast spin-transfer torque driven by femtosecond pulsed-laser excitation. *Nat. Commun.* 5, 4333 (2014).
- Choi, G.-M., Moon, C.-H., Min, B.-C., Lee, K.-J. & Cahill, D. G. Thermal spin-transfer torque driven by the spin-dependent Seebeck effect in metallic spin-valves. *Nat. Phys.* 11, 576–581 (2015).
- Georgieva, Z. N., Bloom, B. P., Ghosh, S. & Waldeck, D. H. Imprinting chirality onto the electronic states of colloidal perovskite nanoplatelets. *Adv. Mater.* 30, 1800097 (2018).
- Huang, Z. et al. Magneto-optical detection of photoinduced magnetism via chirality-induced spin selectivity in 2D chiral hybrid organic-inorganic perovskites. ACS Nano 14, 10370–10375 (2020).

- Kim, Y.-H. et al. Chiral-induced spin selectivity enables a room-temperature spin light-emitting diode. Science 371, 1129–1133 (2021).
- 29. Hu, J., Yan, L. & You, W. Two-dimensional organic–inorganic hybrid perovskites: a new platform for optoelectronic applications. *Adv. Mater.* **30**, 1802041 (2018).
- 30. Long, G. et al. Spin control in reduced-dimensional chiral perovskites. *Nat. Photonics* **12**, 528–533 (2018).
- Lu, H. et al. Spin-dependent charge transport through 2D chiral hybrid lead-iodide perovskites. Sci. Adv. 5, eaay0571 (2019).
- 32. Choi, G.-M. & Cahill, D. G. Kerr rotation in Cu, Ag, and Au driven by spin accumulation and spin-orbit coupling. *Phys. Rev. B* **90**, 214432 (2014).
- Schulz, L. G. The optical constants of silver, gold, copper, and aluminum. I. The absorption coefficient k. J. Opt. Soc. Am. 44, 357–362 (1954).
- McLaughlin, R., Sun, D., Zhang, C., Groesbeck, M. & Vardeny, Z. V. Optical detection of transverse spin-Seebeck effect in permalloy film using Sagnac interferometer microscopy. *Phys. Rev. B* 95, 180401 (2017).
- 35. Cahill, D. G. Analysis of heat flow in layered structures for time-domain thermoreflectance. *Rev. Sci. Instrum.* **75**, 5119–5122 (2004).
- Liu, J. et al. Simultaneous measurement of thermal conductivity and heat capacity of bulk and thin film materials using frequency-dependent transient thermoreflectance method. Rev. Sci. Instrum. 84, 034902 (2013).
- Zhang, L. & Niu, Q. Angular momentum of phonons and the Einstein-de Haas effect. Phys. Rev. Lett. 112, 085503 (2014).

- 38. Ren, Y., Xiao, C., Saparov, D. & Niu, Q. Phonon magnetic moment from electronic topological magnetization. *Phys. Rev. Lett.* **127**, 186403 (2021).
- 39. Brataas, A., Kent, A. D. & Ohno, H. Current-induced torques in magnetic materials. *Nat. Mater.* **11**, 372–381 (2012).
- 40. Koopmans, B. et al. Explaining the paradoxical diversity of ultrafast laser-induced demagnetization. *Nat. Mater.* **9**, 259–265 (2010).
- 41. Uchida, K. et al. Spin Seebeck insulator. *Nat. Mater.* **9**, 894–897 (2010).
- 42. Vetter, E. et al. Tuning of spin-orbit coupling in metal-free conjugated polymers by structural conformation. *Phys. Rev. Mater.* **4**, 085603 (2020).
- 43. Qian, Q. et al. Chiral molecular intercalation superlattices. *Nature* **606**, 902–908 (2022).
- 44. Das, T. K., Tassinari, F., Naaman, R. & Fransson, J. Temperature-dependent chiral-induced spin selectivity effect: experiments and theory. *J. Phys. Chem. C* **126**, 3257–3264 (2022).

Publisher's note Springer Nature remains neutral with regard to jurisdictional claims in published maps and institutional affiliations.

Springer Nature or its licensor (e.g. a society or other partner) holds exclusive rights to this article under a publishing agreement with the author(s) or other rightsholder(s); author self-archiving of the accepted manuscript version of this article is solely governed by the terms of such publishing agreement and applicable law.

© The Author(s), under exclusive licence to Springer Nature Limited 2023

Methods

Synthesis of materials

R-MePEAI and S-MePEAI. Before reaction with the chiral amine, unstabilized hydroiodic acid (57 wt% in water, Sigma-Aldrich) was purified using a 0.36 M tributyl phosphate solution in chloroform, following a previously reported procedure⁴⁵. Then, fresh purified hydroiodic acid (1.9 ml) was added dropwise into a cold solution of *R*-MePEA or S-MePEA (2 ml; 98+%, TCI America) in ethanol (5 ml) under stirring in an ice bath. After 1 h of stirring, the crude product was obtained by slowly evaporating the solvent under a reduced pressure. Then the white–light yellow precipitate was dissolved and recrystallized in ethanol and washed with diethyl ether three times. The product was dried under vacuum overnight and kept in a nitrogen-gas-filled glove box for further use.

Deposition of perovskite films and device fabrication. Boron-doped p-type single-side-polished (100) Si substrates (University Wafer) with a resistivity of 1–10 Ω cm were cleaned using ultrasonic waves in deionized water, acetone and then 2-propanol for 15 min each. The substrates were dried under a stream of nitrogen and subjected to treatment with ultraviolet-ozone for 15 min. For the *R*- or *S*-MePEAI-based perovskite, the precursor solution was made by dissolving *R*- or *S*-MePEAI and PbI₂ in dimethylformamide at the molar ratio of *R*- or *S*-MePEAI:PbI₂ = 2:1 and the solution was stirred at room temperature for 1 h. The concentration of Pb²⁺ was 0.3 M. The 2D perovskite film was obtained by spin-coating the precursor solution at 5,000 revolutions per min for 20 s onto a precleaned Si substrate followed by thermal annealing at 80 °C for 30 s.

After the thin-film preparation, a 50-nm-thick Cu layer was deposited on top of the thin film for the spin accumulation detection. For the STT samples, the 2D chiral HOIP thin film was spun-cast onto the Si substrate using the same recipe, followed by a 50-nm-thick Cu spacing layer and a 15-nm-thick NiFe top layer, deposited using electron-beam evaporation. All the sample surfaces were verified as smooth surfaces (root mean squared roughness < 15 nm) for optical measurements (Supplementary Fig. 3).

TDTR measurements. Before the TDTR measurements, an ~80-nm-thick Al thin film and a 10-nm-thick Cu thin film were deposited on the samples via electron-beam evaporation. For the TDTR, a mode-locked Ti:sapphire laser (Tsunami, Spectra Physics) produced a train of pulses at a repletion rate of 80 MHz. The temporal width of each pulse was 250 fs; the spectrum of pulses was centred at 785 nm with a FWHM (full-width at half-maximum) of ≈10 nm. A mechanical delay stage was used to change the optical path difference between the pump and probe beams before they were focused through an objective lens onto the sample surface. The pump beam was modulated at a frequency f_{mod} so that the thermoreflectance change at the sample surface could be detected by the probe beam via lock-in detection. The radius of the focused Gaussian laser beams was ≈6 µm. The laser power on the sample surface could be adjusted and measured accurately. Further details on the TDTR can be found elsewhere³⁶ and in the Supplementary

TR-MOKE measurements. The TR-MOKE methodology was used to detect the transient spin signals. The experimental setup was the same as for the TDTR setup except that a different detection scheme was used (see our previous work⁴⁶). The incident probe was linearly polarized; the rotation of the polarization on reflection from the sample surface was measured by splitting the probe beam using a Wollaston prism and detecting the changes in the intensity of the orthogonal polarization states using a balanced detector. The pump beam was modulated and the detection using a lock-in amplifier still applies here. To prevent degradation during the

measurements, the samples were placed in a vacuum chamber with optical access (ARS-DMX-20-OM). The vacuum pressure was kept below at least 10^{-6} mbar during the measurements. A neodymium (NdFeB) permanent magnet was fixed outside the chamber to apply the external magnetic field if needed. The accurate field strength was measured using a Gaussmeter. The data were averaged over multiple scans (-10–50) to increase the signal-tonoise ratio.

Data availability

Source data are provided with this paper. The source data for the Supplementary Information are available from the corresponding author upon reasonable request.

References

- 45. Smith, I. C., Hoke, E. T., Solis-Ibarra, D., McGehee, M. D. & Karunadasa, H. I. A layered hybrid perovskite solar-cell absorber with enhanced moisture stability. *Angew. Chem. Int. Ed.* **53**, 11232–11235 (2014).
- 46. Liu, J., Choi, G.-M. & Cahill, D. G. Measurement of the anisotropic thermal conductivity of molybdenum disulfide by the time-resolved magneto-optic Kerr effect. *J. Appl. Phys.* **116**, 233107 (2014).

Acknowledgements

J.L. acknowledges the financial support from the National Science Foundation under award number CBET 1943813 for the ultrafast measurements, thermal characterizations and thermal modelling. D.S. acknowledges the financial support provided by the US Department of Energy, Office of Science, under the grant number DE-SC0020992 for the device fabrications. D.S. and W.Y. acknowledge the support through the Center for Hybrid Organic-Inorganic Semiconductors for Energy (CHOISE), an Energy Frontier Research Center funded by the US Department of Energy, Office of Science, Office of Basic Energy Sciences for material synthesis, thin-film preparations and magnetic characterizations. J.L. acknowledges partial financial support from the North Carolina Space Grant New Investigator Award for the student aids. D.S. and J.L. also acknowledge the partial financial support from the North Carolina State University Research and Innovation Seed Funding for the student aids. The X-ray diffraction of the perovskite thin films in this work was performed at the Chapel Hill Analytical and Nanofabrication Laboratory (CHANL), a member of the North Carolina Research Triangle Nanotechnology Network (RTNN), which is supported by the National Science Foundation, grant ECCS-1542015, as part of the National Nanotechnology Coordinated Infrastructure (NNCI). The circular dichroism measurements were performed at the UNC Macromolecular Interactions Facility supported by the National Cancer Institute of the National Institutes of Health under award number P30CA016086.

Author contributions

D.S., J.L. and W.Y. conceived the experiments and supervised this research. K.K., C.Y. and Z.W. were responsible for the ultrafast TR-MOKE and TDTR measurements. E.V., L.Y. and A.C. fabricated the samples. X.L., J.L., L.Z. and J.Z. provided the theoretical models. Y.Y. and J.L. calculated the spatial and temporal temperature profile. C.Y. and R.S. conducted the magnetization dynamics and spin current density analysis. D.S. and J.L. wrote the manuscript. All authors contributed to editing the manuscript.

Competing interests

The authors declare no competing interests.

Additional information

Supplementary information The online version contains supplementary material available at https://doi.org/10.1038/s41563-023-01473-9.

Correspondence and requests for materials should be addressed to Lifa Zhang, Wei You, Dali Sun or Jun Liu.

Peer review information *Nature Materials* thanks Yossi Paltiel and the other, anonymous, reviewer(s) for their contribution to the peer review of this work.

Reprints and permissions information is available at www.nature.com/reprints.